THE ASTROPHYSICAL JOURNAL, 425:568–581, 1994 April 20

EVIDENCE FOR TWO CLASSES OF PARSEC-SCALE RADIO DOUBLE SOURCE IN ACTIVE GALACTIC NUCLEI

J. E. CONWAY
National Radio Astronomy Observatory, Socorro, NM 87801

AND

S. T. MYERS, T. J. PEARSON, A. C. S. READHEAD, S. C. UNWIN, AND W. XU
Owens Valley Radio Observatory, Mail Code 105-24, California Institute of Technology, Pasadena, CA 91125
Received 1993 August 18; accepted 1993 October 13

ABSTRACT

There is a group of powerful compact radio sources which have two almost equal flux density components on parsec scales. On the basis of multifrequency, multiepoch VLBI observations, we conclude that there are two physically distinct classes among such sources.

In one class the two components are probably "minilobes" where oppositely directed jets terminate. Because of their intrinsic symmetry we believe the new name "compact symmetric objects" best describes this class of object. We present detailed observations of the source 0108+388, showing that this source has properties consistent with this class, including a very small limit on relative internal motions of $\lesssim 0.18\ h^{-1}\ c$ (using $H_0 = 100\ h$ km s^{-1} Mpc^{-1} and $q_0 = 0.5$). We also detect a weak feature between the two main components which may be associated with the central engine in this source.

We believe there exists another class of double source composed of core-jet sources in which a component in the jet is as bright as the component associated with the central engine. These sources are distinct from those of the first class in showing systematic differences in the properties of the two components. All these sources have small relative motions between the two main components (e.g., in 2021+614 we detect a motion of $0.13\ h^{-1}\ c$ and in 0711+356 an upper limit of $0.4\ h^{-1}\ c$). The combination of large relative brightness for the secondary and the low velocities might be explained if the secondary is due to a bright standing shock in the jet. Alternatively, the bright secondary component might be due to a relativistic flow close to the line of sight at a point along a curving parsec-scale channel (as has been proposed for 4C 39.25).

Subject headings: galaxies: active — galaxies: individual (0108+388) — galaxies: jets — radio continuum: galaxies

1. INTRODUCTION

Most of the powerful compact radio sources that have been studied by the VLBI technique consists of a bright, compact, flat-spectrum radio core and a weaker one-sided "jet" of emission. This structure is thought to be due to the presence of a relativistic parsec-scale jet which is oriented close to the line of sight. However, there is also a small fraction (i.e., comprising approximately 5% of flux-limited samples at 5 GHz) of enigmatic compact objects which do not easily fit the above picture. Phillips & Mutel (1982) first identified objects which consisted of two components of comparable brightness and size and with similar spectra separated by tens of milliarcseconds. Phillips & Mutel (1982) termed this new class of objects "compact doubles." Later observations showed that many of these objects also had other properties in common in addition to their VLBI morphology, which distinguished them from core-jet sources. These properties (Hodges & Mutel 1987) included (1) little or no radio variability (2) a peaked radio spectrum with a maximum in the gigahertz range (see O'Dea, Baum, & Stanghellini 1991a), and (3) no detectable kiloparsec-scale structure.

The slight differences in morphology and spectra in the components of compact doubles rule out gravitational lensing in most cases. Phillips & Mutel (1982) used the similarities in flux density between the two components as an argument against their relativistic separation, a conclusion later confirmed by multiepoch VLBI observations (e.g., Tzioumis et al. 1989; Conway et al. 1992). Compact doubles have been interpreted by models in which the two components mark regions in which twin parsec-scale jets terminate within the nucleus of the host galaxy (Phillips & Mutel 1982). These objects might therefore be considered to be very small analogs of the "classical double" sources. There small size might arise because the jets in these objects have only recently been activated and so have not had time to burrow their way out of the galactic nucleus; they could be sources in which an especially dense nuclear environment has kept the source small and confined; or they could represent a new class of powerful short-lived radio galaxies—which is the interpretation we favor (Readhead et al. 1994).

While there are objects having all the properties of compact doubles as defined by Hodges & Mutel (1987), there are others which show only some of these properties and some properties of core-jet sources. The physical nature of these sources has been unclear. An example is 0711+356 (see § 4), which is a double on VLBI scales, has little or no internal motion and a somewhat peaked radio spectrum, yet shows significant radio variability. In the 5 GHz complete sample defined by Pearson & Readhead (1988), out of 37 objects bright enough to be imaged with Mk II (narrow-band) VLBI, only three objects were VLBI doubles with all of the properties of the compact double class as defined by Hodges & Mutel (1987). However, there were additionally four objects (including 0711+356) which were VLBI doubles yet showed only some of the defin-

ing properties. In separating the two groups of sources, the main distinguishing feature was the steepness of their radio spectra above their spectral peak. The first group of sources had a steep spectral index (i.e., $\alpha \approx -1$, where $S \propto \nu^{\alpha}$), while the second group had a flatter index ($\alpha \approx -0.5$ or larger), hence the two groups of sources were identified (Pearson & Readhead 1988) as "compact S doubles" and "compact F doubles," respectively.

We have been engaged in multiepoch, multifrequency VLBI observations of both subclasses of VLBI double sources as part of our continuing study of the Pearson-Readhead (PR) survey. One major objective has been to understand better the place of the compact F doubles in the phenomenology of radio sources. Another objective has been to test the predictions of the "terminating jet" model for the compact S doubles. In a previous paper (Conway et al. 1992) we discussed in detail two of the compact S doubles (namely, 0710+439 and 2352+495) and found that their properties were consistent with this model. In this paper we report VLBI observations of a further three VLBI doubles drawn from the PR survey, one a compact S double, the others compact F doubles. Observations of the "S"-type source (0108+388; see § 3) show it to be consistent with the terminating jet model. In contrast, observations of 0711+356 (see § 4), 2021+614 (see § 5), and other compact F doubles drawn from the literature (see § 6.1) suggest that these objects are unusual forms of "core-jet" source.

TABLE 1

JOURNAL OF OBSERVATIONS OF 0108+388

Characteristic	5.011 GHz	4.989 GHz	10.7 GHz	4.991 GHz
Epoch	1976.56	1982.94	1984.11	1986.90
Duration (hr)	12	6 (Bonn) 10 (US)	8 (Bonn) 12 (US)	4 × 1
Antennas[a]	GFOH	BKGFO	BKGO	SJBWKGFYO

[a] See Table 3, note a.

2. VLBI OBSERVATIONS AND DATA REDUCTION

2.1. *Observations*

The details of the VLBI observations are given in Tables 1–3 for each of the target sources. Experiments used antennas from both the European VLBI network (EVN) and the US VLBI network. The maximum resolution was approximately 4 mas at 1.7 GHz, 1 mas at 5 GHz, and 0.5 mas at 10.7 GHz.

All observations were made with left-circular polarization (IEEE convention), and a bandwidth of 1.8 MHz was recorded using the Mk II format (Clark 1973). The data were cross-correlated with the JPL/Caltech VLBI Correlator. The data were fringe-fitted in the AIPS package, and the 2 s data points averaged over periods of about 1 minute; error bars for the averaged data were estimated from the internal scatter of the data over the averaging interval. After amplitude calibration (Cohen et al. 1975), maps were made using the self-calibration algorithms of Readhead & Wilkinson (1978) and Cornwell & Wilkinson (1981) as implemented in the Caltech VLBI package (Pearson 1991). Gaussian model fits were made to the visibility data at each epoch, fitting the observed amplitude and closure phase directly. In all cases it was possible to obtain excellent fits to the data (i.e., reduced χ^2 or "agreement factors" less than 1.3 in both amplitude and closure phase) using only a few Gaussian components.

2.2. *Multiepoch Intercomparison*

A major objective of our multiepoch 5 GHz observations was to detect or set limits on temporal changes within our target sources. In general, estimating such changes using maps or model fits made independently at the two epochs is unreliable because of differences in data reduction and aperture

TABLE 2

JOURNAL OF OBSERVATIONS OF 0711+356

Characteristic	5.011 GHz	10.651 GHz	4.989 GHz	10.649 GHz	4.991 GHz
Epoch	1980.53	1981.43	1982.92	1984.10	1986.89
Duration (hr)	7 (Bonn) 10 (US)	9	4 (Bonn) 3 × 4 (US)	4 (Bonn) 12 (US)	4 × 1
Antennae[a]	BKGFO	BKGO	BKGO	BKGO	SJBWHKGFYO

[a] See Table 3, note a.

TABLE 3

JOURNAL OF OBSERVATIONS OF 2021+614

Characteristic	5.009 GHz	10.651 GHz	1.661 GHz	4.989 GHz	4.991 GHz
Epoch	1979.91	1982.44	1982.76	1982.93	1987.74
Duration (hr)	12	11	10 8 (Bonn)	9	4 × 1
Antennas[a]	KGFO	BKGFO	BKGIYOHP	BKGFO	SJBWLKGIFY27HO

[a] S—26 m, Onsala Space Observatory, Onsala, Sweden. J—25 m, Mk II telescope, Jodrell Bank, Cheshire, UK B—100 m, Max-Planck-Institut für Radioastronomie, Effelsberg, Germany. W—14 × 25 m, Phased Array, Westerbork Synthesis Radio Telescope, The Netherlands. L—32 m, Medicina, Italy, K.—36.6 m, Haystack Observatory of the Northeast Radio Observatory Corporation, Westford, MA. G—42.7, National Radio Astronomy Observatory, Green Bank, WV. I—18.3 m, North Liberty Radio Observatory of the University of Iowa, North Liberty, IA. F—26 m, George R. Agassiz Station of Harvard University, Fort Davis, TX. Y—25 m, one antenna of the NRAO Very Large Array, Socorro, NM. Y27—27 × 25 m, Phased Array, NRAO Very Large Array, Socorro, NM. O—40 m, Owens Valley Radio Observatory of the California Institute of Technology, Big Pine, CA. H—25.9 m, Hat Creek Observatory of the University of California, Cassel, CA. P—25.6 m, Dominion Radio Astrophysical Observatory, Penticton, BC, Canada.

coverage at each epoch (Conway et al. 1992). A much better procedure is to compare the visibility data at the two epochs. However, complications arise because of small differences in aperture coverage at each epoch due to precession, nutation, and slight differences in observing frequency (see Tables 1–3). To overcome these problems, we used a procedure in which we first found a Gaussian model which fitted the data at one epoch to within the thermal noise. The Fourier transform of this Gaussian model was then compared with the visibility data at another epoch and any differences noted. The use of a model made it possible to interpolate between the small differences in aperture coverage.

If changes in sources structure were indicated, we attempted to characterize their nature by model fitting to the second-epoch data using the first-epoch components as a starting model. In most cases we began by allowing only component amplitudes to change; then, step by step, we varied component positions and shapes. If a significant change in a property of a component was found (e.g., its position), we tested its reliability by fixing this property and allowing all other parameters of all other components to vary. Only if the best agreement factor thus obtained was significantly worse than in the original did we feel confident in claiming that the data supported the change. Our criterion for a "significantly worse" fit was one on which the agreement factor was worse by 10% or more. Finally, to remove possible effects due to errors in amplitude calibration, we investigated the effects of amplitude-self-calibrating the data at one epoch with the model from the other epoch before model fitting. This procedure could remove or reduce real changes. In some cases we estimated the degree of such biasing using simulated data.

In most cases the above method of interepoch comparison was carried out twice. In the first approach the model from the first epoch was fitted to the data set from the second epoch after editing out data which was not common to both epochs. In the second approach all the data from the second epoch was used. While the first approach eliminates biases due to different aperture coverage, it often leaves a relatively small amount of data. In practice we found that the two approaches gave similar results (see §§ 3.3, 4.3, and 5.3). This gave us confidence in the detected structural changes and showed that having identical aperture coverage at each epoch is not essential if a good model is available.

3. OBSERVATIONS

3.1. *Previous Observations*

The source of 0108+388 is identified with a galaxy at a redshift of 0.6690 (C. Lawrence 1993, private communication). Recently r and i-band optical imaging (Stanghellini et al. 1993) have revealed a slightly asymmetric galaxy which is very red ($r - i = 1.2$ mag). The nucleus is also much more prominent in the i than in the r band—suggesting possible nuclear obscuration.

At radio wavelengths 0108+388 is a classic gigahertz peaked spectrum (GPS) object with a spectral turnover near 5 GHz (Herbig & Readhead 1992). Above the spectral turnover the spectral index is steep ($\alpha = -1.27 \pm 0.14$ between 5 and 22 GHz; O'Dea, Stanghellini, & Baum 1991b). It was this steep spectral index which led Pearson & Readhead (1988) to classify this source as a compact S double. Below the spectral turnover, $\alpha = +2.1 \pm 0.1$ (between 318 and 365 MHz; O'Dea et al. 1991b), one of the steepest optically thick spectral indices measured in any source and comparable to the theoretical spectral index of 2.5 expected for a simple homogeneous synchrotron self-absorbed component.

Radio observations show that this source has no detectable polarization (i.e., $\leq 0.2\%$) at both 1.4 and 5 GHz (Perley 1982). These is no evidence for radio variability in this object (Seielstad, Pearson, & Readhead 1983; Aller, Aller, & Hughes 1992). A first-epoch 5 GHz VLBI map (using US stations only, with resolution 2.9 mas × 2.1 mas; Pearson & Readhead 1988) showed that the source consisted of two, almost equal-brightness, similar-sized components with separation 5 mas. VLBI polarization observations (Cawthorne et al. 1993) failed to detect any polarized structure in this source and yielded upper limits of 4 mJy on the polarized flux density.

The object 0108+388 was the first compact double to show evidence for radio structure on kiloparsec scales (Baum et al. 1990). Using the Westerbork Synthesis Radio Telescope (WSRT) at 6 and 49 cm and the VLA at 20 cm, a weak feature was detected 20″ to the east of the parsec-scale double. This detection casts doubt on the young classicial double interpretation (Phillips & Mutel 1982). Baum et al. (1990) suggest that the kiloparsec- and parsec-scale structure might instead be explained by either recurrent activity or a jet which has recently been "smothered" by the infall of dense gas onto the nucleus.

3.2. *Multifrequency VLBI Imaging*

Figures 1*a* and 1*b* show the highest quality 5 GHz images of 0108+388 (made from the third-epoch data). Figure 1*c* shows the 10.7 GHz image. As is common in many other compact double sources, the separation in centroids of the two components is larger at the higher frequency (Mutel, Hodges, & Phillips 1985), even when the images are convolved to the same resolution. This could be due to a spectral gradient within the source, with flatter spectrum emission at the edges; alternatively, it could be due to diffuse trailing tails of emission in each component which are inadequately represented in the higher frequency image.

The 10.7 GHz image shows evidence of a component with a flux density of 28 mJy between the two main components. We tried to window out this central component and self-calibrate without this feature, but in all cases it reappeared in our images. Because of the lower resolution of our 5 GHz maps, we cannot confirm or rule out the presence of such a component at this lower frequency.

A comparison at 5 and 10.7 GHz of the total flux density in the eastern and western components (excluding the region where the middle component was found) gave $\alpha = -1.09$ and -1.72 for the eastern and western components, respectively. The large derived spectral index for the western half of the source is almost certainly due to some of the diffuse emission detected at 5 GHz being resolved out at 10.7 GHz.

On the basis of the maps, we can derive physical parameters for different parts of the radio source. We find that all of these parameters, e.g., minimum pressures, magnetic fields, are largest at the leading edge of the eastern component. From equipartition arguments (Moffet 1975) we determine from the 5 and 10.7 GHz maps that the largest magnetic field there is about 0.1 G. In contrast, the synchrotron self-absorption arguments give a smaller field of 0.01 G, suggesting that the radio plasma is particle-dominated. Minimum pressures in this region are in the range (4–9) × 10^{-4} dyn cm^{-2}. Given its size, this source is probably embedded in the narrow-line region

(NLR) of its host galaxy. Assuming an NLR intercloud medium with particle density $10^{4\pm1}$ cm^{-3} and temperature 10^6 K (Netzer 1991), static pressure is therefore a factor of 10^4 too small to confine the radio components. On the other hand, given the assumed NLR density, if the two components are the analogs of the lobes of classical double sources, then their leading edges could be confined if their advance speeds were in the range $0.02c$–$0.25c$. The predicted inverse Compton X-ray emission from 0108+388 is dominated by the contribution from the eastern component. Using the formula of Marscher (1983), a size estimate of FWHM 0.6 mas × 0.2 mas, a high-frequency spectral index of unity, and a minimum cutoff frequency to the spectrum at 100 GHz, we estimate that the 1 keV X-ray flux density should be 0.004 μJy. The upper limit as quoted in a footnote within Biermann et al. (1987) is 0.01 μJy. The present limits are therefore consistent with a model which has no bulk relativistic motion of, or within the eastern lobe.

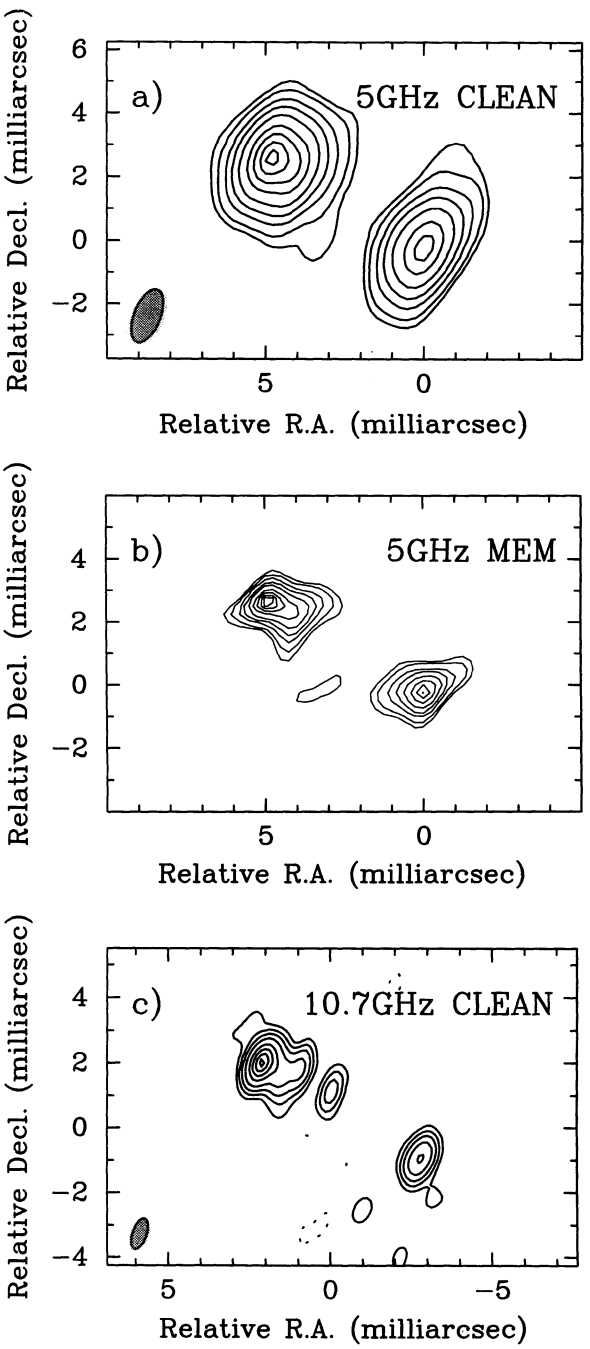

FIG. 1.—Images of 0108+388. (*a*) CLEAN image at 5 GHz, from third-epoch data. Beam FWHM size is 1.81 × 0.86 mas in P.A. −21°.9. Peak flux density is 430 mJy beam^{-1}. Contour levels are at 1, 2, 5, 10, 20, 40, 60, 80, and 95% of peak. (*b*) MEM image at 5 GHz, from third-epoch data. Pixel spacing is 0.125 mas. Peak brightness is 51 mJy pixel^{-1}. Contour levels are at 1, 2, 5, 10, 20, 40, 60, 80, and 95% of peak. (*c*) CLEAN image at 10.7 GHz, from first-epoch data. Beam FWHM size is 0.93 × 0.44 mas in P.A. −21°.4. Peak flux density is 176 mJy beam^{-1}. Contour levels are at −2, 2, 5, 10, 20, 40, 60, 80, and 95% of peak.

3.3. *Multiepoch Monitoring*

We have three epochs of observations at 5 GHz spanning 6 years and are able to investigate possible temporal changes within this source. However, because the first-epoch data involved only US stations, we concentrate on comparisons between the second and third epochs. We find that the third-epoch Gaussian model provides an excellent fit to the second-epoch data, suggesting minimal changes between these two epochs. However, the positions of deep visibility minima are very sensitive to source structure changes. Figure 2 shows fits to deep minima in the second-epoch data of versions of the third-epoch model in which the separations of the two Gaussians comprising the eastern component are shifted relative to the two Gaussians in the western component by between −50 and +50 μas. Figure 2 shows that the χ^2 of the fits is asymmetric with respect to a shift in the relative separation and that the best fit occurs for shifts of between 0 and −50 μas in the third-epoch separation, corresponding to an increase of separation between epochs 2 and 3 of between 0 and +50 μas.

A similar small shift is indicated by model-fitting tests in which a third-epoch starting model (with agreement factors to the third-epoch data of 1.2 and 1.1 in amplitude and closure phase, respectively) is adjusted to fit the second-epoch data. We carried out an exhaustive series of such tests (see § 2.2). In all cases an increase in the separation of the centroids of the eastern and western components was indicated. In cases in which we fitted the model only to the "overlapping" visibility data (i.e., only second-epoch data having common aperture coverage with the third-epoch data), we find that the two compact Gaussians in the eastern feature moved outward relative to the most compact Gaussian in the western feature by about 35 and 20 μas, respectively. In contrast, when fitting to the full data at the second epoch, we found that a similar net increase in centroid separation of about 35 μas could be obtained with a relative motion between the two Gaussians comprising the western half of the source. We also found that if the second-epoch data were first amplitude–self-calibrated against the third-epoch model before fitting, then the magnitude of the required centroid shift was reduced by only 20%–30%. This test demonstrates that the shift is not due to an artifact of differences in amplitude calibration at the two epochs.

From the above model-fitting results, it seems likely that a small increase in centroid separation has occurred. A shift of 35 μas in centroid position over the 3.96 yr between epochs 2 and 3 corresponds to a separation velocity of 0.18 h^{-1} c; it is interesting that this is comparable to the values required for ram-pressure confinement found in § 3.2. However, as shown by the different results when fitting to "overlapping" and "full" data at the second epoch, it is impossible to characterize

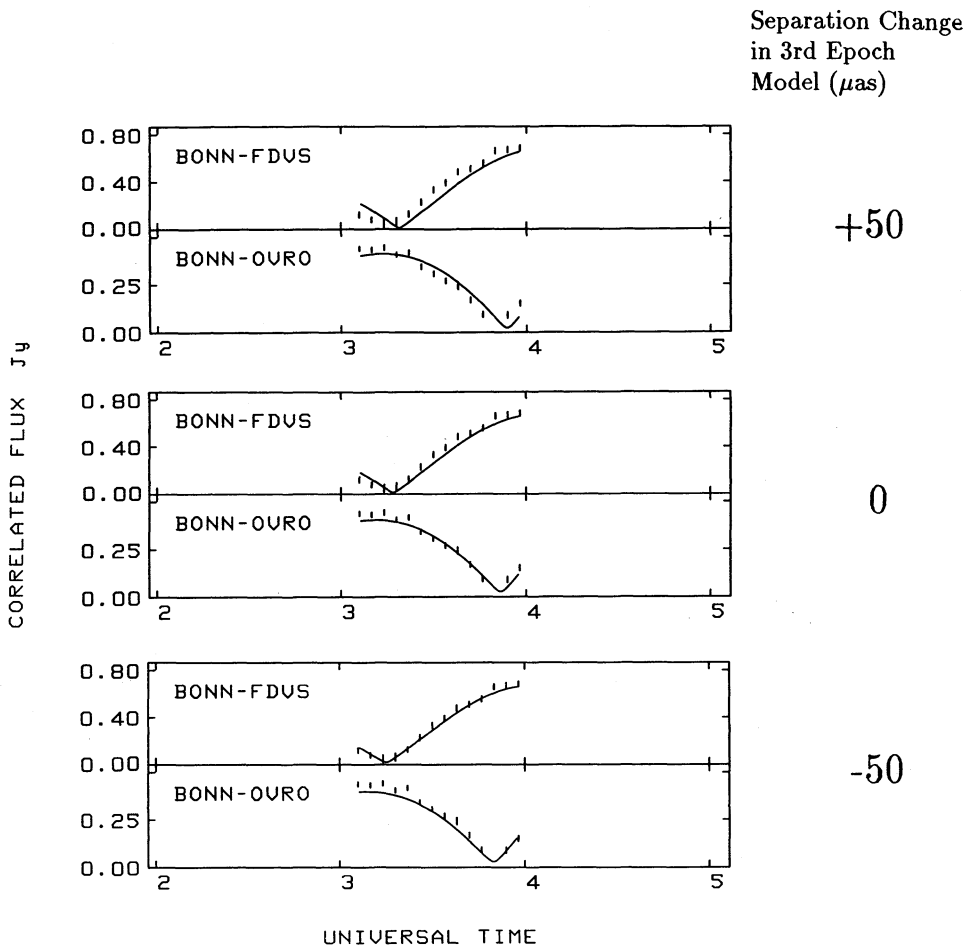

FIG. 2.—Illustration of a possible change in 0108+388 between epochs 2 and 3. Middle panel shows fit of third-epoch model to second-epoch data. Top and bottom panels show the fit of versions of the third-epoch model in which the separation of the two main components is respectively increased and decreased by 50 μas. Note that the goodness of fit is asymmetric with respect to changes in separation, with the best fit occurring for a change of between 0 and −50 μas, corresponding to an *increase* in component separation between epoch 2 and epoch 3.

uniquely the nature of the structural changes that may have occurred. While the data can be explained by an overall expansion of the source, other possibilities exist, such as a change in the brightness of the putative middle component, which we discussed in § 3.2. Given these uncertainties, we can only reliably quote an upper limit of 0.18 h^{-1} c on the separation velocity of the two main components.

4. OBSERVATIONS OF 0711+356

4.1. *Previous Observations*

The source 0711+356 is a quasar at redshift 1.62 (Hewitt & Burbidge 1987). The radio spectrum of this object (see Herbig & Readhead 1992) shows a broad maximum, peaking around 2 GHz. Above the spectral turnover (between 5 and 10.7 GHz) $\alpha > -0.5$, and hence this object was classified by Pearson & Readhead (1988) as a compact F double. At radio wavelengths this source shows weak but detectable polarization (i.e., 0.8% and 1.6% at 5 and 1.4 GHz, respectively; Perley 1982). Quirrenbach et al. (1992) report that this source shows radio variability at a level of about 5% during observations lasting a few days. On longer time periods, Aller et al. (1992) report significant variations in flux density during the period 1985–1991 at both 5 and 15 GHz.

High dynamic range 1.4 GHz VLA observations have revealed kiloparsec-scale structure in this object (Murphy, Browne, & Perley 1993). Two compact features are detected on roughly opposite sides of the nucleus, 4″ and 8″ away, respectively. First-epoch 5 GHz VLBI observations (Pearson & Readhead 1988) showed this source to be a double with separation of about 5 mas and flux-density ratio of approximately 2:1: VLBI polarization observations (Cawthorne et al. 1993) show that the northern of the two main components is 2.6% polarized at 5 GHz, while the southern component has a fractional polarization of less than 2.5%.

4.2. *Multifrequency VLBI Imaging*

This source has been observed at three epochs at 5 GHz and two epochs at 10.7 GHz (see Table 2). The best-quality CLEAN images at each frequency are shown in Figures 3*a* and 3*c*. In the MEM image of the 5 GHz data (Fig. 3*b*) components appear superresolved; however, the resulting structure is entirely consistent with the CLEAN image at 10.7 GHz (Fig. 3*c*).

In all maps and model fits the southernmost feature is most compact, being unresolved at 5 GHz and probably unresolved at 10.7 GHz. The spectrum of this feature between 5 and 10.7 GHz is slightly inverted (i.e., $\alpha = +0.12$). In contrast, the main

secondary component to the north is resolved even at 5 GHz and is steep-spectrum ($\alpha = -0.82$) between 5 and 10.7 GHz. The images and model fits at 5 GHz also suggest some diffuse emission to the west of the northern component; this emission is not seen at 10.7 GHz. However, at both frequencies we do see emission linking the two main components. In all cases this "bridge" emission lies to the west side of the line joining the two main components.

The spectrum and compactness of the southern component suggest that this component is the "core," or nucleus, of the radio source. If we asume this and take the northern feature as being part of a radio jet, then we find that this source has a large-jet-to-counterjet ratio, i.e., 220:1 as measured by the peak brightness, or 130:1 as measured by the total flux density on each side.

4.3. *Multiepoch Comparisons*

The biggest change in this source appears to be a systematic decrease in the flux density of the northern component over the 6.4 yr time span of the VLBI monitoring. Extensive model-fitting tests comparing the first- and third-epoch 5 GHz data, using both overlapping and total data and with and without cross-amplitude self-calibration (see § 2.2), all gave consistent results—a decrease in the flux density of the main northern component by about 40%. The second epoch gave a flux density for this component intermediate between its values at epochs 1 and 3. We also found that the flux density of the northern component in the 10.7 GHz images decreased by about 20%–30% between the first and second epochs. Because of differences in aperture coverage and the effects of spectral index, it is unclear whether the flux density of this component increased or decreased between the first-epoch 5 and 10.7 GHz observations.

In contrast to these flux density changes, for the most part the changes in component positions required by multiepoch model fitting are relatively small. Over the large ensemble of model-fitting experiments comparing the first- and third-epoch 5 GHz data, we found that the biggest change in the separation between the southern component and the main Gaussian in the northern component was a separation decrease of only 70 μas. Treating this shift as an upper limit on any motion, this suggests that the mean radial separation velocity of these two components between epochs 1 and 3 must be below $0.4\ h^{-1}\ c$. Such a limit is also consistent with intercomparisons between the first and second epoch and between the second and third epoch. The 5 GHz data set also show maximum changes in the position angle of the vector between the southern and main northern components of less than 0°.7 corresponding to transverse shifts of less than 70 μas.

Intercomparison of the two 10.7 GHz epochs again gave small limits on the change in the *radial* separation between southern and northern components (i.e., less than 50 μas). However, in these 10.7 GHz data there does appear to be evidence of significant *transverse* shift in the centroid of one of the two components. This change is apparent both in the image plane and in the Greenwich sidereal times of amplitude minima on the longest baselines. If we register on the southern component a comparison of Figures 4*a* and 4*b* shows that the centroid of the northern component moves sideways by about 0.5 beamwidth. The difference map (Fig. 4*c*) reveals that the centroid shift is almost entirely due to a decrease in emission of a feature on the eastern edge of the northern component. Comparing the position of centroids of the northern component over all the data at both 10.7 and 5 GHz, we find a signature in which the northern component first moves to the east between the first 5 and 10.7 GHz epochs (i.e., between 1980.53 and 1981.43), then moves back toward the west over the next three epochs (1982.92, 1984.10, and 1986.89). Conway & Murphy (1993) have shown that under certain conditions component centroids can move sideways if a bright shock feature moves

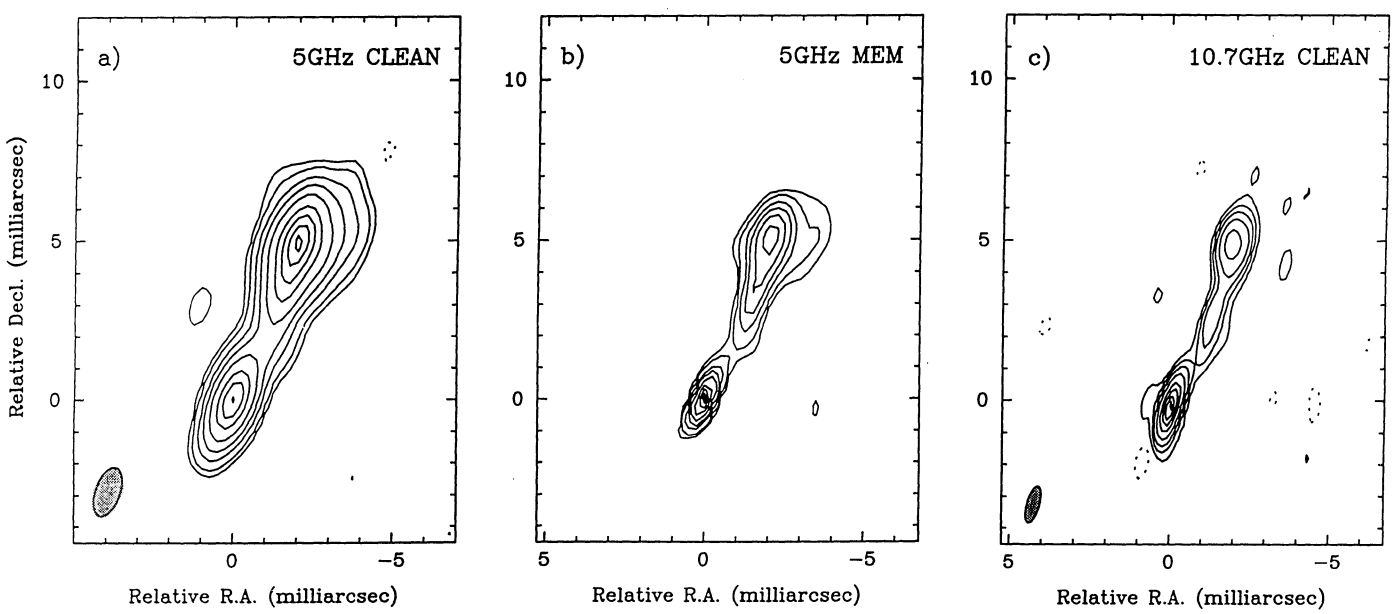

FIG. 3.—Images of 0711+356. (*a*) CLEAN image at 5 GHz, from third-epoch data. Beam FWHM size is 1.61 × 0.80 mas in P.A. −18°.9. Peak flux density is 263 mJy beam^{-1}. Contour levels are at 1, 2, 5, 10, 20, 40, 60, 80, and 95% of peak. (*b*) MEM image at 5 GHz, from third-epoch data. Pixel spacing is 0.25 mas. Peak brightness is 40 mJy pixel^{-1}. Contour levels are at 1, 2, 5, 10, 20, 40, 60, 80, and 95% of peak. (*c*) CLEAN image at 10.7 GHz, from first-epoch data. Beam FWHM size is 1.20 × 0.40 mas in P.A. −21°.4. Peak flux density is 179 mJy beam^{-1}. Contour levels are at −2, 2, 5, 10, 20, 40, 60, 80, and 95% of peak.

along a twisting parsec-scale jet and passes through a highly beamed region where the jet tangent is close to the line of sight. Both the large flux density changes and the structural change (see Fig. 4) seen within the northern component at 10.7 GHz would be consistent with such a model.

Considering next the "bridge" emission, we note that CLEAN maps made independently using data at each 5 GHz epoch (see Conway et al. 1991) apparently showed a motion northward of the peak in the "bridge" emission of about 0.5 mas between epochs 1 and 3. Such a shift would correspond to a velocity $2.9\ h^{-1}\ c$ if the components at each epoch are the same. However, in the second-epoch 5 GHz map the position of the peak in the bridge was similar to that in the first epoch; furthermore, no significant shift of this feature was detected between the two 10.7 GHz epochs. Careful model-fitting analysis comparing the first- and third-epoch 5 GHz data has shown that equally good fits can be obtained if this middle feature is allowed to move or is fixed relative to the southern component. In fact, the position of the middle feature appears to be poorly constrained by the available data, so we conclude that changes in the bridge structure are not required by the data, but are not ruled out either.

To summarize: We find definite evidence for significant change in the flux density of the northern component. This is probably associated with a change in its shape; however, there appears to be no signifiant outward motion of the component. There are also possible changes in the emission between the two main components, but these are poorly constrained. While we cannot be exactly sure of the nature of the changes that have occurred, this compact F double definitely shows much more structural variation than is seen in compact S doubles such as 0108+388 (see § 3.3).

5. OBSERVATIONS OF 2021+614

5.1. *Previous Observations*

The source 2021+614 has been identified with an elliptical galaxy with a redshift of 0.2266 (Bartel et al. 1984b). Deep *R*-band CCD imaging (O'Dea, Baum, & Morris 1990) shows that this galaxy has a prominent, compact nucleus and two possible companions within 12″.

The radio spectrum is relatively flat from 0.7 to 10.7 GHz (Herbig & Readhead 1992). Based on this flat spectrum above the turnover, Pearson & Readhead (1988) classified this object as a compact F double. At higher frequencies the spectrum steepens ($\alpha \approx -0.8$ between 20 and 90 GHz). However, Steppe et al. (1988) report a flux density measurement at 230 GHz which is larger than at 90 GHz, suggesting an upturn in the spectrum at very high frequencies. This source shows no structure on scales larger than 0.″2 at levels of 0.3 mJy beam^{-1} or above (Perley 1982) and has very low polarization (i.e., $\lesssim$0.1% at 5 GHz). Seielstad et al. (1983) report a 20% change in flux density on a 10 year timescale at 10.6 GHz. Aller et al. (1992) also detect some variability over a 5 year timescale at 15 GHz but not at 4.8 GHz.

Bartel et al. (1984a) presented the results of simultaneous VLBI observations at 2.3 and 8.4 GHz. At both frequencies the emission is dominated by two components separated by about 7 mas. At the lower frequency two further components, almost collinear with the main components are visible. In this discussion we adopt Bartel's convention and name the components A, B, C, and D starting from the northeast and proceeding southwest (see Fig. 5*b*). The observations showed that between 2.3 and 8.3 GHz the bright southwest component (D) has an inverted spectrum, while the other bright northeast component (B) has a flat spectrum. The VLBI flux measurements and the overall spectrum of the source are consistent (Bartel et al. 1984*a*) with each of the two main components having simple synchrotron self-absorbed spectra which peak at different frequencies. VLBI polarization imaging by Cawthorne et al. (1993) found no significant polarized flux from any of the components (upper limit 5 mJy).

5.2. *Multifrequency Mapping*

This source has been observed at three frequencies: 10.7, 5, and 1.7 GHz (see Table 3). At 10.7 GHz only two components

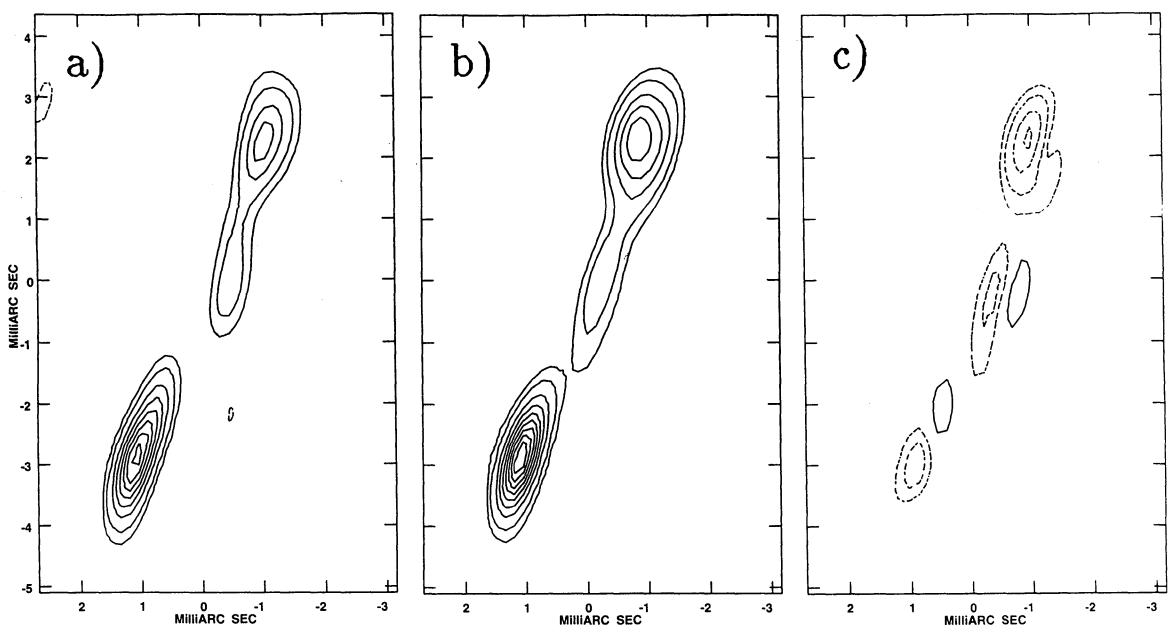

FIG. 4.—Difference between 0711+356 images at the two 10.7 GHz epochs. The images are registered on the southern component. In all cases the CLEAN beam has FWHM 1.2 × 0.4 mas in P.A. −15°. Contour levels are at −60, −40, −20, −10, 10, 20, 40, 60, 80, 100, 120, 140, and 160 mJy beam^{-1}. (*a*) 1984 image. (*b*) 1981 image. (*c*) Difference between 1984 and 1981 images.

1994ApJ...425..568C

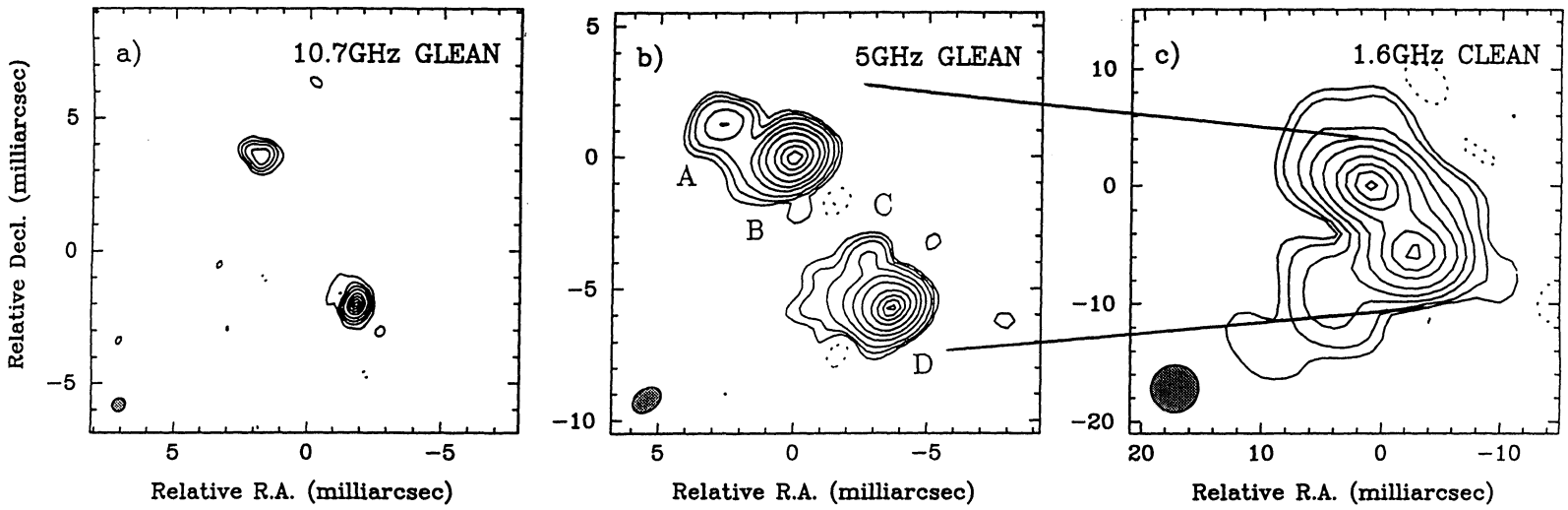

FIG. 5.—Images of 2021+614. (*a*) CLEAN image at 10.7 GHz. Beam FWHM size is 0.5 mas circular. Peak flux density is 643 mJy beam^{-1}. Contour levels are at −2, 2, 5, 10, 20, 40, 60, 80, and 95% of peak. (*b*) CLEAN image at 5 GHz, from the third-epoch data. Beam has FWHM 1.19 × 0.82 mas with P.A. −52°6. Peak flux density is 724 mJy beam^{-1}. Contour levels are at −0.5, 0.5, 1, 2, 5, 10, 20, 40, 60, 80, and 95% of peak. (*c*) CLEAN image at 1.6 GHz. Beam FWHM size is 4 mas circular. Peak flux density is 674 mJy beam^{-1}. Contour levels are at −1, 1, 2, 5, 10, 20, 40, 60, 80, and 95% of peak.

are detected, namely, B and D (see Fig. 5*a*), with component D being much brighter than component B. Component D is also more compact than B: Gaussian fitting to the image gives deconvolved FWHMs of 0.52 × 0.28 mas and 0.63 × 0.47 mas for D and B, respectively. The best 5 GHz observations were made in epoch 3 (see Fig. 5*b*) when 13 stations observed over four scans each an hour long. The structure is still dominated by the same two components seen at 10.7 GHz, but both mapping and model fitting now reveal the two additional components (A and C) found at 2.3 GHz by Bartel et al. (1984a). However, in our 5 GHz map there is also some evidence of weak diffuse emission to the southwest of component C. The 1.7 GHz map (Fig. 5*c*) show a more extensive "tail" leading in the same direction as the extension seen at 5 GHz. At the resolution limit of this map the emission from components A and B cannot be separated, nor can that from C and D, and the main body of the source therefore appears as an almost equal double comprising emission from features (A + B) and (C + D).

Figure 6 shows the overall spectrum of 2021 + 614 together with flux densities of the individual components. The component flux densities at 5 and 10.7 GHz are taken directly from our own observations (see Figs. 5*a* and 5*b*), while those at 2.3 and 8.3 GHz come from Bartel et al. (1984a). Although at 1.7 GHz, because of limited resolution, we can only measure (see Fig. 5*c*) the combined flux densities of (A + B) and of (C + D) at this frequency we expect the contributions of components B and D to be small compared to those of A and C. In plotting estimates of the 1.7 GHz flux density of A and C, we have removed estimates of these small B and D flux densities by using model spectra fitted to their higher frequency data.

We have attempted to fit the spectra of each component with the simple synchrotron self-absorbed spectrum expected from a homogeneous cloud of plasma and magnetic field (van der Laan 1966). In this simple case the low-frequency (optically thick) spectral index is always 2.5, while the high-frequency (optically thin) spectral index is a free parameter. The other two free parameters are the flux density and frequency at which the spectral turnover occurs.

Of the two components which dominate at 5 and 10.7 GHz, namely, B and D, we find that B has the lower turnover frequency and has a spectrum that falls off relatively fast (i.e., with spectral index −1.25) at frequencies above 5 GHz. In contrast, component D must have a much broader spectrum, both to account for the VLBI measurements and to explain the overall source spectrum above 10.7 GHz. Although our combined model spectra still underpredicts the total flux density in the range 10–30 GHz, this can be accounted for by a systematic variation in the flux density of D between the epoch of the total flux measurements (late 1970s, early 1980s) and that of the VLBI measurements (mid- to late 1980s). It is known (see § 5.3) from multiepoch VLBI imaging that component D shows epoch-to-epoch flux density variations of order 25%. Variability in D is also possibly indicated by the anomalously low 8.3 GHz flux density from Bartel et al. 1984a).

Turning to consider components A and C, we find that in order to fit their measured 2.3 and 5 GHz flux densities we require very steep (i.e., spectral indices −2.0 and −2.25 respectively) high-frequency spectra. In these two components there is also the suggestion that spectra are more curved than can be accounted for by synchrotron self-absorbed spectra and that there may be a steepening at high frequency (possibly indicative of spectral aging of electrons due to synchrotron losses). The low-frequency (at less than 1.7 GHz) behavior of the spectra of components A and C is somewhat uncertain, although the total source spectrum constrains both components to peak above 1 GHz.

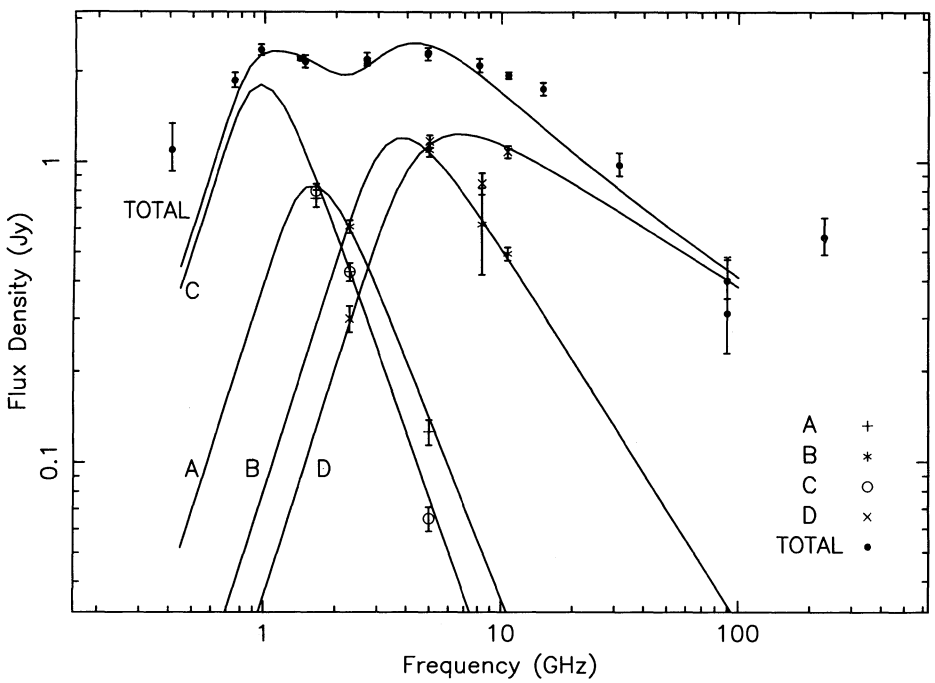

FIG. 6.—Radio spectrum of 2021 + 614 and a possible spectral decomposition (see § 5.2). Measurements of total flux density (*filled circles*) come mainly from Kühr et al. (1984) and references therein. Additional points are from Gregorini et al. (1984) (408 MHz) and from Steppe et al. (1988) (90 and 230 GHz). Measurements of flux density of the four main VLBI components (see Fig. 5) come from our own observations at 1.7, 5, and 10.7 GHz. At 2.3 and 8.3 GHz the measurements come from Bartel et al. (1984a). The solid lines show model SSA spectra for each of the four main components, and the sum of these individual spectra (see § 5.2 for details).

Based on our multifrequency VLBI observations, we interpret component D as being associated with the central engine in this source. This interpretation is based on component D being the most compact feature, having the highest turnover frequency and the broadest spectrum, and being the most variable component (see § 5.3). The other features, A, B, and C, we identify with a radio jet. Support for a core-jet interpretation also comes from the results of multiepoch monitoring (see § 5.3). It is unclear how to interpret the diffuse "tail" seen at 1.7 GHz (see Fig. 5*c*). One possibility is that it is the counterjet, in which case the jet-counterjet ratio calculated on the basis of the peak brightness in the jet and counterjet is 20:1. The large misalignment between the jet and the counterjet could easily be explained by projection effects. A more speculative possibility is that the lowest contour in Figure 5*c* delineates a cone of emission with its apex near component D. A helical jet wrapped around this cone might give bright spots (namely, A + B and C + D) at points where the jet is oriented close to the line of sight.

5.3. *Multiepoch Data Analysis*

Since the first-epoch 5 GHz data contained only four US stations and no global baselines (see Table 3), we concentrate on comparing the second- and third-epoch data. Comparing visibility data common to both the second and third epochs, we find significant differences between the epochs. If we start with the third-epoch model and allow the amplitudes of the different components to vary, the best fit is obtained if component D increases in flux density by about 40%, while the flux densities of the other components increase by factors of approximately 15%. These changes are therefore consistent with a difference in the absolute flux density scale at the two epochs of about 15%, and a real increase in the flux density component of D of about 25%.

Note, however (see Fig. 7*a*), that the fit after allowing component flux density variations is still relatively poor, especially on the transatlantic baselines. Particularly on the Bonn-OVRO baseline there appears to be a significant change in the spacing of the amplitude minima, suggesting motions between the source components. Allowing the amplitudes of all components to vary, but only component D to move, we immediately get a greatly improved fit (see Fig. 7*b*). Furthermore, the change in the position of component D is directly away from the other components in going from epoch 2 to epoch 3 (i.e., increasing separation with time). A similar shift of component D relative to the other components is obtained if all Gaussian parameters including shapes are allowed to vary simultaneously. However, a good fit could not be obtained if the position of the southern component was fixed or if we allowed changes only in Gaussian shapes but not in positions.

We found similar position shifts if we fitted to the total data at epoch 2 or just to the visibility data common to both epochs (see § 2.2). In the former case the relative shift between components A and C was 53 μas, while in the latter case the required shift was 69 μas. Assuming 1 degree of freedom per hour per antenna, the decrease in χ^2 gave an estimated random error of 12 μas on the position of component D, so that the observed shift is statistically significant. We tried to eliminate the observed position shift by first amplitude–self-calibrating the epoch 2 data by the epoch 3 model before model fitting. For overlapping data this procedure reduced the required shift from 69 to 33 μas. However, when we simulated two epochs of 2021 + 614 data with a shift of 69 μas between them, we found that by amplitude–self-calibrating one data set against the model at the other epoch we could reduce the apparent shift to a similar value, namely, 30 μas. It therefore appears that the behavior of the real data is consistent with a true shift of order 69 μas.

We have tested and ruled out models in which an apparent shift in centroids between the two main components is generated by changes in the relative brightness of internal subcomponents within component D. We found that in order to give the observed shift and be consistent with only a 25% change in flux density of the whole of component D, the separation and flux densities of the two subcomponents would be large enough to show up in our model fitting. In trying to represent D with only a single Gaussian when in reality it contained two components, our agreement factors would be limited to about 8 (compared to the value of 1.3 achieved for the third epoch). Overall it seems more likely that the apparent centroid shift represents motion between the two main components in the sources. Assuming the shift is 69 μas in the 4.81 yr between epochs 2 and 3, the apparent outward separation velocity between the two components is 0.13 h^{-1} c.

6. INTERPRETATION AND CONCLUSIONS

6.1. *Source Classification*

Combining the results in this paper with other published data, we now have available high-quality VLBI observations of all seven of the objects from the PR sample (Pearson & Readhead 1988) which were classified as parsec-scale doubles. We can now attempt to draw conclusions about the nature of these objects, which do not seem to fit easily the core-jet parsec-scale morphology seen in most compact radio sources. As noted in § 1, Pearson & Readhead subdivided the parsec-scale doubles into two subclasses based on the steepness of their high-frequency spectra. One class was termed "compact S doubles" because, although they had spectral peaks, their high-frequency spectral indices were $\alpha < -0.5$; "compact F doubles" had high-frequency spectral indices $\alpha > -0.5$ above their spectral peaks. This subdivision appears to be a useful one, since, as discussed below, it appears to be correlated with differences in parsec-scale structures and other properties.

The sole compact S double discussed in this paper is 0108 + 388. Of the three objects discussed, it is the least like a core-jet source and the most similar to the compact double sources as first defined by Phillips & Mutel (1982). The narrowness of its radio spectral peak argues that both of the two major components must have spectra which peak at very similar frequencies. Although the eastern feature is slightly more compact than the western one, both main components contain structure on several scales; neither appears as a simple unresolved "core" of emission. Furthermore, of all the PR sources with bright parsec-scale emission, this object appears to be the least variable in total flux density and has a very small limit on internal transverse velocities (see § 3.3). In fact, all the physical parameters derived in § 3.2 seem to be consistent with the terminating jet model. It is also notable that, except for its smaller size, this object is morphologically similar (see § 6.2) to the two other Pearson-Readhead survey compact S doubles, 0710 + 439 and 2352 + 495 (Conway et al. 1992), both of which are well described by the terminating jet model. It apears that these three PR objects have similar VLBI morphologies and form a well-defined subclass of compact radio sources which

1994ApJ...425..568C

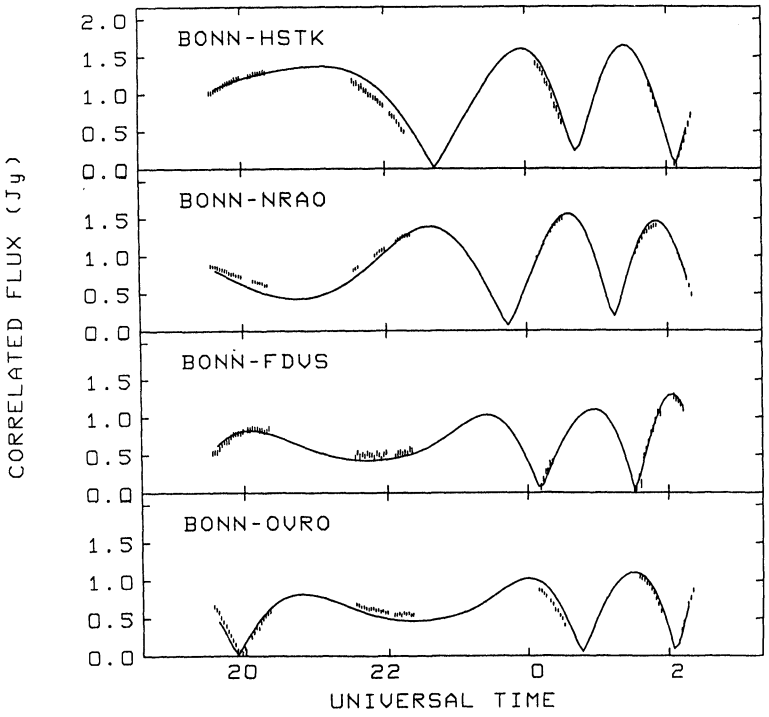

FIG. 7a

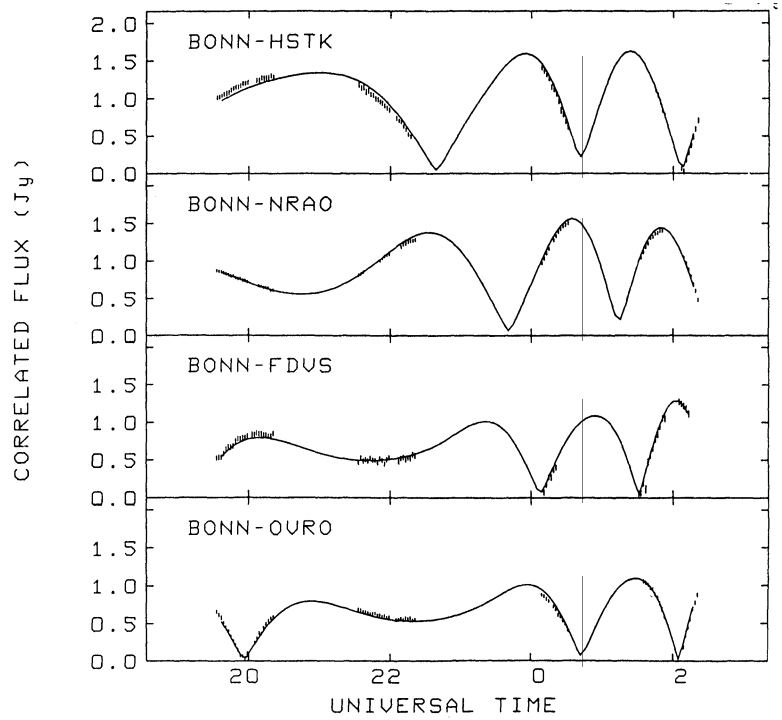

FIG. 7b

FIG. 7.—Evidence for a subluminal motion in 2021+614. Diagrams show the results of model fitting to the second epoch 5 GHz 2021+614 data starting with the best third-epoch Gaussian model. (*a*) Amplitude fit on transatlantic baselines after allowing only amplitudes of Gaussian components to vary. (*b*) Fit after allowing component amplitudes and position of southernmost component (D) to vary. Note that second-epoch data are plotted only at GST times at which there were also third-epoch data.

we term "compact symmetric objects." We discuss these objects further in § 6.2.

We now consider the compact F doubles, i.e., those two-component objects having high-frequency spectra with $\alpha > -0.5$. As explained in §§ 4 and 5, both of the compact F doubles 0711+356 and 2021+614 show a progression of properties from one end of the source to the other which suggest that their VLBI components are bright features within a one-sided jet. In 0711+356 the southern component has a flat spectrum between 5 and 10.7 GHz and is much more compact than the northern component, being unresolved even at 10.7 GHz (see § 4.2). Likewise, in 2021+614 the southern component is more compact than the main northern feature and has a broader radio spectrum which peaks at a higher frequency (see § 5.2). The southern component also appears to be the site of the observed changes in total flux density (see § 5.3). It is interesting that the other two PR compact F doubles, namely, 0153+744 (Hummel et al. 1988) and 4C 39.25 (Alberdi et al. 1993; Marscher et al. 1991) also seem to be best described as unusual forms of core-jet source. The source 0153+744 seems to be similar to 0711+356 in many ways, with two major components joined by a curved "bridge" of emission. One of the two main components is compact, while the other is extended, with the more compact component having a higher turnover frequency. The source 4C 39.25 consists of two stationary components with a component moving from west to east between them. The two stationary components can be interpreted as being analogous to the two main components in 0153+744, 0711+356, and 2021+614 (which also show no, or very small, relative motions). The middle component in 4C 39.25 would be a bright version of the bridge emission seen in 0153+744 and 0711+356. Although there is a wider variety of structures among the compact F doubles than among the compact S doubles, we believe that there are enough similarities to group them together as their own distinct subclass of jet source.

Based on the above arguments, the major conclusion of this paper is that there are two types of parsec-scale double. One class is the compact S doubles, which have steep high-frequency radio spectra and symmetrical VLBI structure. We believe that the two outer components in such objects are "minilobes" formed at the termination of two oppositely directed jets within the galactic nucleus. We discuss these objects further in § 6.2. The other class is the compact F doubles, which generally show flatter high-frequency spectra and which we believe are associated with an apparently one-sided radio jet. We discuss further the properties and possible models for such objects in §§ 6.3 and 6.4.

6.2. *Compact S Doubles*

Among the three PR objects in this class we have found that at least two (0710+439 and 2352+495; Conway et al. 1992) and also possibly 0108+388 (see Fig. 1*c* and § 3.2) actually have a *triple* structure. We have good evidence (at least for the first two sources) from spectra, compactness, variability (Conway et al. 1992), and overall symmetry (Wilkinson et al. 1994) that the middle component is associated with the central engine. Such triple structures are consistent with the "standard model" in which these sources are small analogs of classical double-lobed radio sources, since these also contain middle components associated with the central engine. Unfortunately for the original terminology, it does not appear that the presence of *two* components is a defning characteristic of members of the "compact double" class. We therefore prefer the new term "compact symmetric object" to describe 0108+388, 0710+439, 2352+495, and the objects originally defined as compact doubles by Phillips & Mutel (1982).

An interesting question, yet to be definitely answered, is whether middle components are always found in compact symmetric objects. While most compact symmetric objects in the literature have shown no detectable middle component (e.g., 1518+047, CTD 93, and 2050+364; Mutel et al. 1985), it may be significant that originally two out of three of the PR compact S doubles were also thought to have only two components. With better maps, including higher sensitivity, shorter baselines, or higher resolution, the third component became visible.

If the putative middle component found in 0108+388 is associated with a distinct component (and is not simply a bright feature in a tail of emission leading back from the eastern component), then this feature might be associated with the central engine. The ratio of middle component to outer component flux density at 10.7 GHz would be about 0.06, which is much smaller than the corresponding ratios at 5 GHz for 0710+439 and 2352+495 (i.e., 0.8 and 3.4, respectively; Conway et al. 1992). Published maps of other compact symmetric objects (see Mutel et al. 1985) suggest upper limits on the core ratios in these objects of 0.005 (although in some cases, given the ambiguities of imaging, an upper limit of 0.04 is more realistic; R. Phillips 1993, private communication). It seems probable, therefore, that compact symmetric objects have a wide range of middle-component ratios, similar to the situation with classical double-lobed radio sources. This may be a further indication that compact symmetric objects are, except for their small size, phenomena similar to classical double sources.

6.3. *Compact F Doubles: Properties*

Although their internal asymmetries (see § 6.1) argue that the compact F doubles are forms of "jet" sources, these objects share unusual properties which suggest that they may form their own distinct subclass. One such unusual property is that all four such PR objects have small, usually subluminal, limits on internal velocities between two major components (see §§ 4.3 and 5.3; Alberdi et al. 1993, Hummel et al. 1988). The limits on these velocities are summarized in the second column of Table 4.

These small velocity detections/limits are especially surprising given the significant jet/counterjet ratios in these sources (see the third column of Table 4). Assuming that bulk flow speed and pattern speeds are the same, and that the jets are straight, it is possible to calculate the probability of selecting sources which fit both the jet/counterjet and apparent velocity constraints, using a standard beaming model. For an assumed jet flow speed β a minimum angle to the line of sight θ_0 can be calculated for which these two constraints are fulfilled. Using these values of β and θ_0, and assuming that total flux scales as $\gamma^{-2}(1-\beta\cos\theta)^{-2}$ and the index of the intrinsic source-count distribution is 3/2, we can calculate the probability of selecting sources with $\theta < \theta_0$ within a sample selected by total flux (Murphy 1988).

If it is assumed that the jet β corresponds to $\gamma = 5$, then it can be shown that the probability of satisfying both the velocity and the jet/counterjet constraints is (for sources other than 0153+744) less than 10^{-3}. As the jet β is reduced, the probability increases but reaches a maximum for a β which is just

TABLE 4

PROPERTIES OF COMPACT F DOUBLES

Name (1)	Observed Apparent Transverse v/c, β_{obs} (2)	Jet/Counterpart Ratio R (3)	β for Jet with Highest Probability of $\beta_{app} < \beta_{obs}$[d] (4)	Probability of $\beta_{app} < \beta_{obs}$ (5)
0153+744	$<1.7\ h^{-1}$	>100[a]	>0.95	>0.99
0711+356	$<0.4\ h^{-1}$	>130	0.55	0.06
4C 39.25	$<0.3\ h^{-1}$	>20[b]	0.43	0.43
2021+614	$0.13\ h^{-1}$	>95	0.51	0.04
		20[c]	0.37	0.10

[a] Based on lowest contour of 1.7 GHz map of Hummel et al. 1988.
[b] Based on lowest contour in 8.4 GHz map of Alberdi et al. 1993.
[c] Assuming that diffuse tail is the counterjet (see § 5.2).
[d] In calculating cols. (4) and (5), a minimum value of $\beta \cos\theta = (R^{1/4} - 1)/(R^{1/4} + 1)$ is assumed, where R is the jet/counterjet ratio from col. (3); we also assumed $h = 0.75$.

slightly higher than the minimum allowed by the jet/counterjet ratio. Columns (4) and (5) in Table 4 list respectively the jet velocity at which the probability is maximized and the value of that probability. For both 0711+356 and 2021+614 the probabilities are low even in cases where the jet has its "optimum" internal velocity. The present limits on apparent transverse velocity for 0153+744 and on jet/counterjet ratio for 4C 39.25 are not yet good enough to tell whether there is a similarly low probability of detection in these two sources. Nevertheless, it appears from Table 4 that the standard jet model has difficulty in simultaneously explaining the high jet/counterjet ratios and the low proper motions observed within these objects.

Another unusual feature of these four objects is the large ratio in flux density between the less compact and the more compact components. Although this may be implicit in the definition of objects which are equal doubles, this ratio is much higher than the ratio between jet and core emission in conventional core-jet sources.

Finally, the spectral properties of the compact components within these objects are somewhat unusual for "core" components of conventional "core-jet" sources. In none of the four PR objects does the most compact feature have a simple flat spectrum; instead, the spectrum of the most compact feature is peaked. This is most obvious in the case of 2021+614 (see Fig. 6). In the case of 4C 39.25, multifrequency model fitting (Alberdi et al. 1993) shows that all of the main components have spectral peaks between 8.4 and 22 GHz. In 0153+744 the most compact component has a spectrum with a distinct peak in the 5–10.7 GHz range (Hummel et al. 1988). In 0711+356 a complete spectral decomposition is not possible because of the lack of a published map at 1.7 GHz; however, the overall spectrum suggests that although the southern component is flat between 5 and 10.7 GHz, this probably represents the peak of a spectrum that falls off below 5 GHz and above 10.7 GHz. While core components having peaked radio spectra are not unprecedented, their presence in all four of the jet doubles is unusual.

6.4. *Compact F Doubles: Models*

In one model for compact F doubles, one or more of the bright stationary features in these objects would be due to strong *stationary shocks* in the jet. Such internal shocks might be generated in response to a rapid change in the environment of the jet (Daly & Marscher 1988). This mechanism would naturally explain why there appears to be a correlation between having a strong feature in the jet and the jet being stationary (or very slowly moving). Furthermore, by decoupling pattern speeds and bulk flow speeds, this mechanism can easily explain the large jet/counterjet ratios despite the small apparent velocities. This decoupling would have implications for the interpretation of proper-motion studies (see Vermeulen & Cohen 1994). The somewhat peaked ratio spectrum of the compact component could be explained in this model if it were entirely or partly due to an earlier standing shock in the jet rather than emission only from the core itself. Such repeated shocks are a possibility in the model proposed by Daly & Marscher (1988).

In an alternative model, compact F doubles are generated by *curving or twisting* parsec-scale relativistic jets. In all cases the bright secondary would be seen where the tangent to the jet fluid flow direction comes close to the line of sight, giving rise to highly Doppler-boosted emission. Such a model could naturally explain both the high brightness of the secondary components and why they are stationary. Because a twisting jet samples a range of angles to the line of sight, the simple arguments used in calculating the low probability of detection of objects with the observed proper-motion and jet/counterjet ratios (see § 6.3) would no longer apply. In this model the other main component could be the core itself or highly beamed emission from a earlier turn of the twisting jet. Even in the former case, of core emission, the fact that the jet is bending as it emerges from the central engine might explain the unusual spectral properties of the compact components found in the compact F doubles. The bending flow would emphasize the contribution to the total spectrum from certain parts of the jet and hence destroy the "cosmic conspiracy" which gives rise to a overall flat-spectrum core in straight jets (Blandford & Königl 1979).

There is considerable evidence for the twisting-jet model in at least one of the PR compact F doubles, namely, 4C 39.25, in which a feature can be seen moving between the two stationary components and which has a behavior consistent with this model (Alberdi et al. 1993; Marscher et al. 1991). In 0711+356 the apparent sideways shift of the northern component (see § 4.3) is, under special conditions, just what is expected from Doppler-boosted emission from a twisting jet (Conway & Murphy 1993). The highly bent arclike emission in 0153+744 has been successfully modeled as being due to the jet having a helical path (Hummel et al. 1988). In 2021+614, although there is less direct evidence for the twisting-jet model, it is possible that the diffuse emission seen at 1.7 GHz could trace a helix cone and that the compact features prominent at 5 and

10.7 GHz could be Doppler-boosted emission from a helical channel on the surface of this cone (see § 5.2).

There is now increasing evidence that curved channels are a common property of parsec-scale jets (e.g., Conway & Murphy 1993; Hummel et al. 1992; Venturi et al. 1993; Wrobel & Conway 1993; Zensus 1990). Furthermore, helical distortions have been predicted as arising naturally as a result of Kelvin-Helmholtz instabilities (Hardee 1987). It would therefore not be too surprising if the combination of such twisting jets and Doppler boosting gave rise to a population of sources (comprising the four PR compact F doubles and possibly 3C 395; see Simon et al. 1988) where one or more components corresponded to places where the jet curves directly toward the line of sight.

J. E. C. acknowledges support of a NRAO Jansky Fellowship. Some of this work was also carried out while the author was a Postdoctoral Research Fellow at the California Institute of Technology. S. T. M., T. J. P., A. C. S. R., S. C. U., and W. X. all acknowledge support from NSF grant AST 91-17100. We thank the observatories of the US and European VLBI networks and thank NRAO for use of the VLA, operated by Associated Universities, Inc., under cooperative agreement with the National Science Foundation.

REFERENCES

Alberdi, A., Marcaide, J. M., Marscher, A. P., Zhang, Y. F., Elosegui, P., Gomez, J. L., & Shaffer, D. B. 1993, ApJ, 402, 160
Aller, M. F., Aller, H. D., & Hughes, P. A. 1992, ApJ, 399, 16
Bartel, N., et al. 1984a, ApJ, 279, 116
Bartel, N., Shapiro, I. I., Huchra, J. P., & Kühr, H. 1984b, ApJ, 279, 112
Baum, S. A., O'Dea, C. P., Murphy, D. W., & de Bruyn, A. G. 1990, A&A, 232, 19
Biermann, P. I., Kühr, H., Snyder, W. A., & Zensus, J. A. 1987, A&A, 185, 9
Blandford, R. D., & Königl, A. 1979, ApJ, 232, 34
Cawthorne, T. V., Wardle, J. F. C., Roberts, D. H., Gabuzda, D. C., & Brown, L. F. 1993, ApJ, 416, 496
Clark, B. G. 1973, Proc. IEEE, 61, 1242
Cohen, M. H., et al. 1975, ApJ, 201, 249
Conway, J. E., & Murphy, D. W. 1993, ApJ, 411, 89
Conway, J. E., Pearson, T. J., Readhead, A. C. S., Unwin, S. C., Xu, W., & Mutel, R. L. 1992, ApJ, 396, 62
Conway, J. E., Unwin, S. C., Pearson, T. J., Readhead, A. C. S., & Xu, W. 1991, in Compact Steep Spectrum and GHz-Peaked Spectrum Sources, ed. C. Fanti, R. Fanti, C. P. O'Dea, & R. T. Schilizzi (Bologna: Istituto di Radioastronomia CNR), 157
Cornwell, T. J., & Wilkinson, P. N. 1981, MNRAS, 196, 1067
Daly, R. A., & Marscher, A. P. 1988, ApJ, 334, 539
Gregorini, L., Mantovani, F., Echart, A., Biermann, P., Witzel, A., & Kühr, H. 1984, AJ, 89, 323
Hardee, P. E. 1987, ApJ, 318, 78
Herbig, T., & Readhead, A. C. S. 1992, ApJS, 81, 83
Hewitt, A., & Burbidge, G. 1987, ApJS, 63, 1
Hodges, M. W., & Mutel, R. L. 1987, in Superluminal Radio Source, ed. J. A. Zensus & T. J. Pearson (Cambridge: Cambridge Univ. Press), 168
Hummel, C. A., et al. 1992, A&A, 257, 489
Hummel, C. A., Schalinski, C. J., Krichbaum, T. P., Witzel, A., & Johnston, K. J. 1988, A&A, 204, 68
Kühr, H., Witzel, A., Pauliny-Toth, I. I. K., & Nauber, U. 1984, A&AS, 45, 367
Marscher, A. P. 1983, ApJ, 264, 296
Marscher, A. P., Zhang, Y. F., Shaffer, D. B., & Aller, M. F. 1991, ApJ, 371, 491
Moffet, A. T. 1975, in Stars and Stellar Systems, Vol. 9, Galaxies and the Universe, ed. A. Sandage, M. Sandage, & J. Kristian (Chicago: Univ. Chicago Press), 211
Murphy, D. W. 1988, Ph.D. thesis, Univ. Manchester
Murphy, D. W., Browne, I. W. A., & Perley, R. A. 1993, MNRAS, 264, 298
Mutel, R. L., Hodges, M. W., & Phillips, R. B. 1985, ApJ, 290, 86
Netzer, N. 1991, in Active Galactic Nuclei, ed. J. J.-L. Courvoisier & M. Mayor (Saas-Fée Lecture; Berlin: Springer), 57
O'Dea, C. P., Baum, S. A., & Morris, G. B. 1990, A&AS, 82, 261
O'Dea, C. P., Baum, S. A., & Stanghellini, C. 1991a, ApJ, 380, 66
O'Dea, C. P., Stanghellini, C., & Baum, S. A. 1991b, in Compact Steep Spectrum and GHz-Peaked Spectrum Sources, ed. C. Fanti, R. Fanti, C. P. O'Dea, & R. T. Schilizzi (Bologna: Istituto di Radioastronomia CNR), 34
Pearson, T. J. 1991, BAAS, 23, 991
Pearson, T. J., & Readhead, A. C. S. 1988, ApJ, 328, 114
Perley, R. A. 1982, AJ, 87, 859
Phillips, R. B., & Mutel, R. L. 1982, A&A, 106, 21
Quirrenbach, A., et al. 1992, A&A, 258, 279
Readhead, A. C. S., & Wilkinson, P. N. 1978, ApJ, 223, 25
Readhead, A. C. S., Xu, W., Pearson, T. J., Wilkinson, P. N., & Polatidis, A. 1994, in preparation
Seielstad, G. A., Pearson, T. J., & Readhead, A. C. S. 1983, PASP, 95, 842
Simon R. S., Hall, J., Johnston, J. H., Waak, J. A., & Mutel, R. L. 1988, ApJ, 326, L5
Stanghellini, C., O'Dea, C. P., Baum, S. A., & Laurikainen, E. 1993, ApJS, 88, 1
Steppe, H., Salter, C. J., Chini, R., Kraysa, E., Brunswig, W., & Lobato Perez, J. 1988, A&AS, 75, 317
Tzioumis, A. K., et al. 1989, AJ, 98, 36
van der Laan, H. 1966, Nature, 211, 1131
Venturi, T., Readhead, A. C. S., Marr, J. M., & Backer, D. C. 1993, ApJ, 411, 552
Vermeulen, R. C., & Cohen, M. H. 1994, ApJ, in press
Wilkinson, P. N., Polatidis, A. G., Readhead, A. C. S., Xu, W., & Pearson, T. J. 1994, ApJ, submitted
Wrobel, J. M., & Conway, J. E. 1993, in Sub-arcsecond Radio Astronomy, ed. R. Davis & R. Booth (Cambridge: Cambridge Univ. Press), 236
Zensus, J. A. 1990, in Parsec Scale Radio Jets, ed. J. A. Zensus & T. J. Pearson (Cambridge: Cambridge Univ. Press), 28